Crystal structure of a substrate complex of *myo*-inositol oxygenase, a di-iron oxygenase with a key role in inositol metabolism

Peter M. Brown*†, Tom T. Caradoc-Davies*†, James M. J. Dickson*†, Garth J. S. Cooper*†, Kerry M. Loomes*†, and Edward N. Baker*†‡§

*Maurice Wilkins Centre for Molecular Biodiscovery, †School of Biological Sciences, and ‡Department of Chemistry, University of Auckland, Auckland 1142, New Zealand

Edited by Brian W. Matthews, University of Oregon, Eugene, OR, and approved August 17, 2006 (received for review June 21, 2006)

Altered metabolism of the inositol sugars *myo*-inositol (MI) and D-*chiro*-inositol is implicated in diabetic complications. In animals, catabolism of MI and D-*chiro*-inositol depends on the enzyme MI oxygenase (MIOX), which catalyzes the first committed step of the glucuronate–xylulose pathway, and is found almost exclusively in the kidneys. The crystal structure of MIOX, in complex with MI, has been determined by multiwavelength anomalous diffraction methods and refined at 2.0-Å resolution ($R = 0.206$, $R_{free} = 0.253$). The structure reveals a monomeric, single-domain protein with a mostly helical fold that is distantly related to the diverse HD domain superfamily. Five helices form the structural core and provide six ligands (four His and two Asp) for the di-iron center, in which the two iron atoms are bridged by a putative hydroxide ion and one of the Asp ligands, Asp-124. A key loop forms a lid over the MI substrate, which is coordinated in bidentate mode to one iron atom. It is proposed that this mode of iron coordination, and interaction with a key Lys residue, activate MI for bond cleavage. The structure also reveals the basis of substrate specificity and suggests routes for the development of specific MIOX inhibitors.

diabetes | substrate binding | metalloprotein | HD domain | polyol metabolism

Diabetes mellitus is a chronic disease characterized by hyperglycemia caused by defective action and/or secretion of insulin. Hyperglycemia leads to complications such as nephropathy, neuropathy, retinopathy, and cataract. There is considerable evidence that both type-1 and type-2 diabetes are associated with altered inositol metabolism, particularly of *myo*-inositol (MI) and its less abundant epimeric form, D-*chiro*-inositol (DCI) (1–3). MI is an osmoregulator and a precursor for inositol-based second messengers, and both MI and DCI are known components of endogenous inositol phosphoglycans, which act as insulin mediators (4, 5), leading to the hypothesis that control of inositol levels may have therapeutic potential. Consistent with this hypothesis, administration of inositols, especially DCI and derivatives, lowers blood glucose in diabetes and enhances insulin action (5–7).

The enzyme MI oxygenase (MIOX; EC 1.13.99.1) is a key regulator of inositol levels, catalyzing the first committed step in the glucuronate–xylulose pathway (8, 9), the only known pathway for MI catabolism (10). MIOX is almost exclusively expressed in the kidneys, where it is localized to the proximal tubular epithelial cells (11). Importantly, MIOX also acts on DCI (12) and potentially mediates its catabolism as well. MIOX expression is up-regulated in conditions of hyperosmotic stress (13–14), and in *db*/*db* mice, a model for type-2 diabetes, increased MIOX activity correlates with increased hyperglycemia (13).

MIOX is a 33-kDa nonheme iron protein that catalyzes the oxidative conversion of MI to D-glucuronic acid (15). This reaction (Fig. 1), in which the bond between C6 and C1 of MI is cleaved, involves a dioxygen-dependent four-electron oxidation that appears to be unique in biological systems (9). Recent reports indicate that MIOX activity depends on substrate binding to an antiferromagnetically coupled di-iron center with unusual redox properties and novel catalytic features, distinct from other di-iron oxygenases (16–18). The amino acid sequence of MIOX, which is highly conserved across many species, matches a previously reported mouse renal-specific oxidoreductase (19), indicating that they are the same protein. The sequence bears no obvious similarity to di-iron oxygenases such as ribonucleotide reductase (RNR) (20) or methane monooxygenase (MMO) (21) or to any other protein of known three-dimensional structure. Despite the intense mechanistic interest in MIOX, its evident importance in diabetes, and the possibility that inhibitors of MIOX could be of therapeutic value, little is known of the structure of the enzyme and its di-iron center or the determinants of its substrate binding and specificity.

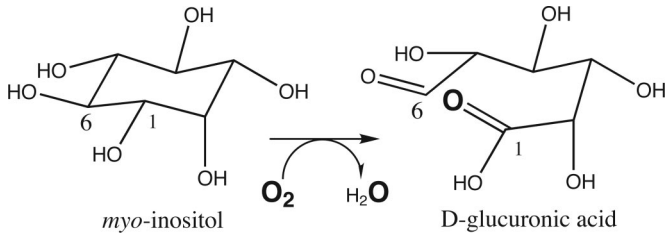

Fig. 1. Reaction catalyzed by *myo*-inositol oxygenase (MIOX).

Here, we describe the 2.0-Å resolution crystal structure of mouse MIOX, in complex with its substrate MI. This structure reveals a mostly helical protein fold, with a distant evolutionary relationship with a widespread protein family referred to as HD domains (22). Crucially, the MI substrate is found to be bound to one of the iron atoms in a manner that gives important clues to the enzyme mechanism and reveals the basis for epimer specificity.

Results

Structure Determination. Mouse kidney MIOX was expressed in *Escherichia coli*, purified, and crystallized in complex with MI, which was essential for obtaining diffracting crystals (23). The enzyme was active when assayed in the presence of 1 mM Fe^{2+} and 2 mM L-cysteine, but the crystals probably represent the inactive, oxidized Fe(III)/Fe(III) form, because of the time required for

Author contributions: J.M.J.D., G.J.S.C., K.M.L., and E.N.B. designed research; P.M.B., T.T.C.-D., and J.M.J.D. performed research; P.M.B., T.T.C.-D., and E.N.B. analyzed data; and K.M.L. and E.N.B. wrote the paper.

The authors declare no conflict of interest.

This paper was submitted directly (Track II) to the PNAS office.

Abbreviations: MI, *myo*-inositol; MIOX, MI oxygenase; DCI, D-*chiro*-inositol; RNR, ribonucleotide reductase; MMO, methane monooxygenase.

Data deposition: The atomic coordinates have been deposited in the Protein Data Bank, www.pdb.org (PDB ID code 2HUO).

§To whom correspondence should be addressed. E-mail: ted.baker@auckland.ac.nz.

© 2006 by The National Academy of Sciences of the USA

Table 1. Data collection and processing statistics

Data collection	Fe peak	Hg peak	Native	Native
Wavelength, Å	1.7389	1.0062	1.0719	0.9795
Resolution range (outer shell), Å	57–2.8 (3.0–2.8)	57–2.4 (2.5–2.4)	57–2.6 (2.7–2.6)	45–2.0 (2.1–2.0)
Total reflections (final shell)	24,632 (3,403)	45,940 (4,849)	31,226 (3539)	243,171 (35,238)
Unique reflections (final shell)	7,448 (1,047)	12,311 (1,587)	9,145 (1,172)	2,0619 (2,954)
Completeness (final shell)	97.1 (95.7)	96.4 (87.6)	95.5 (87.5)	100 (100.0)
Average I/σ (final shell)	15.4 (3.7)	12.8 (3.5)	12.4 (2.3)	18.9 (4.0)
R_{merge} (final shell)	0.060 (0.309)	0.065 (0.223)	0.082 (0.502)	0.087 (0.602)

crystal growth, the aerobic conditions, and the absence of L-cysteine from the crystallization solution. The structure was solved by a single-wavelength anomalous diffraction/single isomorphous replacement with anomalous scattering approach using anomalous scattering from the two intrinsic iron atoms and anomalous and isomorphous differences from a mercury derivative. The structure was then refined at 2.0-Å resolution by using a separate high-resolution data set, to a final R factor of 0.206 (R_{free} = 0.253) (see Tables 1 and 2). No electron density was found for the N-terminal residues 1–28. An N-terminal 3-kDa fragment is readily lost by proteolysis (15), but SDS/PAGE analysis of dissolved crystals (23) showed that the molecule was intact; these residues are assumed to be disordered in the crystal structure. The putative NADPH-binding motif identified by Yang *et al.* (19) is in this disordered region; we find no evidence of NADPH binding (data not shown). The rest of the structure, residues 29–285, has excellent electron density. It conforms well with the Ramachandran plot with 90% of residues in most-favored regions, as defined in PROCHECK (24), and no outliers.

Protein Fold. MIOX is monomeric in solution and in the crystal. It is folded into a single, mostly helical domain (Fig. 2*A*), in which five helices, α4 to α8, form the core and contribute the six ligands of the di-iron center. Helices α4 and α5 (residues 94–111 and 113–132) form an antiparallel pair and contribute three ligands. Two of these, His-123 and Asp-124, constitute the characteristic HD motif of HD-domain proteins (see below) and are found at a point where helix α5 is distorted and its hydrogen bonding is disrupted. Helices α6 and α7 (residues 193–206 and 210–220) form a second antiparallel pair and contribute two more ligands, and helix α8, residues 236–256, completes the di-iron site, contributing the sixth ligand; this helix, too, has its hydrogen bonding disrupted, by the presence of Pro-244. Four more helices decorate the protein surface (Fig. 2*A*): α1 packs against two loops (residues 83–93 and 135–143) that are important for substrate specificity; α2 packs against α7, antiparallel to it; and α3 and α9 lie over the α4–α5 antiparallel pair. In this way, the core helices α4–α7 are largely buried.

Residues 134–190, between helices α5 and α6, form an extensive series of loops that emanate from the main core of the structure. MIOX copurifies from kidney with D-glucuronate reductase, the next enzyme in the MI catabolic pathway (25), and this region, which contains a number of conserved residues distant from the active site, may play a role in protein–protein interactions. Arg-29, immediately following the disordered N-terminal region, has a key structural role, π-stacking with Tyr-31 and forming a salt bridge with Asp-142 that secures the substrate-binding pocket. These three residues are almost completely conserved across >40 putative MIOX sequences. The C-terminal residues 283–285 form a short antiparallel β-ribbon with residues 69–71, with the final residue, Trp-285, inserting its side chain into the hydrophobic core. From residue 29 to 285, the MIOX molecule is well defined, with no obviously mobile regions.

Di-Iron Site. The di-iron site in MIOX (Fig. 3*A*) is buried between two pairs of antiparallel helices, α4/α5 and α6/α7, and a fifth helix, α8. A key feature relevant to the antiferromagnetic coupling of the two iron atoms (16) is that they are doubly bridged, by the carboxylate group of Asp-124, which binds symmetrically through Oδ1 and Oδ2 and by a bridging water or hydroxide that had positive difference density at 6σ in an omit map. The Fe–Fe distance is 3.65 Å, similar to distances observed in other dinuclear iron sites (26). Mutation of Asp-124 to Ala gives colorless, inactive protein, suggesting loss of iron binding. In native MIOX, FE(1) is coordinated by His-98 Nε2, His-123 Nε2, Asp-124 Oδ2 and Asp-253 Oδ1, a water molecule OW-305, and the bridging water/hydroxide OW-304, in a distorted octahedral geometry. FE(2) is also octahedrally coordinated, by Asp-124 Oδ1, His-194 Nε2 and His-220 Nε2, the bridging water/hydroxide and two oxygen atoms, O1 and O6 of the MI substrate. Iron–ligand distances are all in the range 1.99–2.14 Å (see Table 3, which is published as supporting information on the PNAS web site). Assuming that both irons are Fe(III), the resultant 6+ charge is balanced by only 2− from the protein ligands (four His and two Asp). This 4+ net charge on the di-iron site implies that the bridging species is likely to be a hydroxide ion rather than water. We also favor hydroxide over a μ-oxo species because the Fe–OW-304 bond lengths average 2.0 Å, significantly longer than the value of ≈1.8 Å expected for a μ-oxo species (27), and because the bridging oxygen is only 2.70 Å from the noncoordinated carboxylate oxygen Oδ2 of Asp-253, in perfect position to hydrogen bond to it.

Substrate Binding. The bound MI substrate is almost completely buried in a pocket formed between the di-iron site, two short sections of polypeptide (residues 140–142 and 220–223), and a hairpin loop (residues 83–93), which acts as a lid over the substrate and appears to play a critical role in substrate binding. Key interactions that hold the lid in place include three salt bridges, Asp-85/Lys-127, Asp-88/Lys-257, and Asp-92/Arg-39, together with main-chain hydrogen bonds with Thr-32, Arg-39, and Gln-136.

Table 2. Phasing and refinement statistics

Phasing (AUTOSHARP)	
Hg (×7) phasing power (ano/iso)	1.375/1.173
Fe (×2) phasing power (ano/iso)	0.531/0.369
Overall figure of merit	0.462
Refinement (45–2.0 Å resolution)	
No. of reflections, working/test	19,516/1,057
R (outermost shell)	0.206 (0.274)
R_{free} (outermost shell)	0.253 (0.282)
Protein atoms	1,942
Subtrate atoms	12
Ions	2 Fe^{3+}, 1 formate
Water molecules	155
rms deviations, bonds/angles	0.021 Å/1.7°
Average B factor, Å^2	25.1

BIOCHEMISTRY

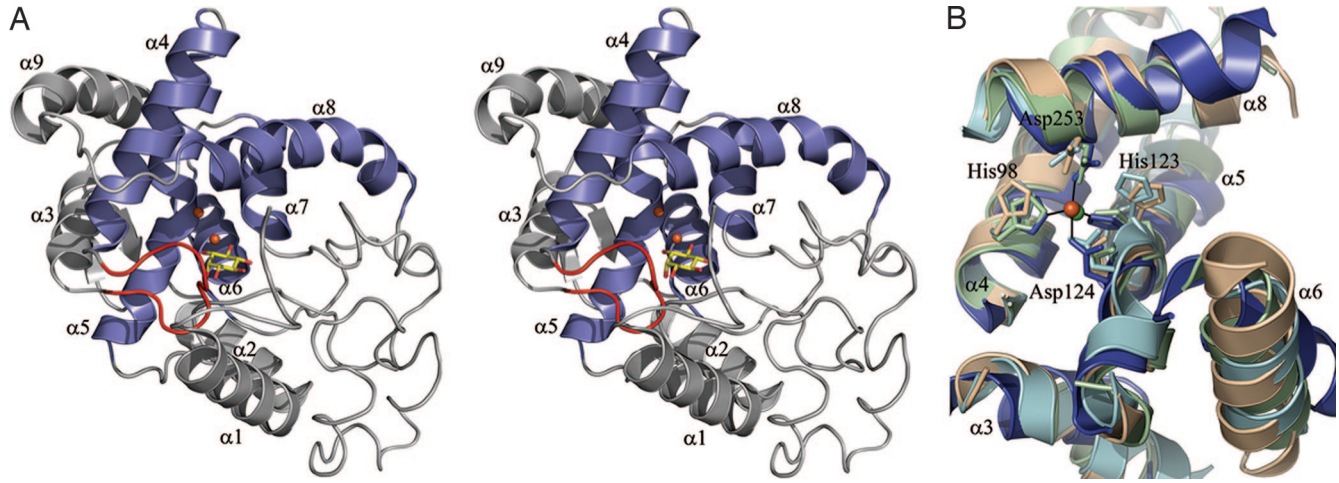

Fig. 2. Structure of MIOX. (*A*) Stereo ribbon diagram, with Fe atoms as orange spheres and MI in yellow, in stick mode. Helices are labeled α1–α9, with the helices that provide iron ligands in blue: the helix pairs α4/α5 and α6/α7 plus α8. The ''lid'' loop that folds over the MI substrate is in red. (*B*) Superposition of common regions of MIOX (dark blue) on the HD domain proteins from *P. furiosus* (green), *A. fulvida* (light blue), and *E. coli* (wheat). The Ni^{2+} ion in the *P. furiosus* protein (green sphere) overlaps FE(1) in MIOX (orange sphere), and equivalent His and Asp residues (stick mode) are present in all four proteins.

Most of these residues are invariant in all MIOX sequences, and the conserved sequence motif DxSDPD (residues 85–90) signifies the importance of this "lid loop" for function.

The electron density for the MI molecule (Fig. 3*B*) is extremely well defined, making its stereochemical fit unequivocal. Of critical importance to the catalytic mechanism, the two oxygens bound to iron are from the C1 and C6 hydroxyl groups, and thus bracket the bond (C1–C6) that is cleaved in the MIOX enzymatic reaction. Both oxygens are also hydrogen bonded to protein groups, O1 to the amino group of Lys-127, invariant in all MIOX sequences, and O6 to Ser-221, conserved in all but one of the 40 MIOX sequences examined. Recognition of the other hydroxyl groups on the inositol ring is achieved by a network of hydrogen bonds. O2 is hydrogen bonded to Asp-85 Oδ1, Ser-87 Oγ, and the peptide NH of Gly-141; O3 to Ser-87 Oγ and water OW-40, which bridges to the side-chain oxygens of Tyr-31 and Tyr-44; O4 to Asp-142 Oδ1 and two waters, OW-40 and OW-66, the latter bridging to Arg-29 Nη1; and O5 to Asp-142 Oδ1. Residues Asp-85, Ser-87, and Asp-142, which medi-

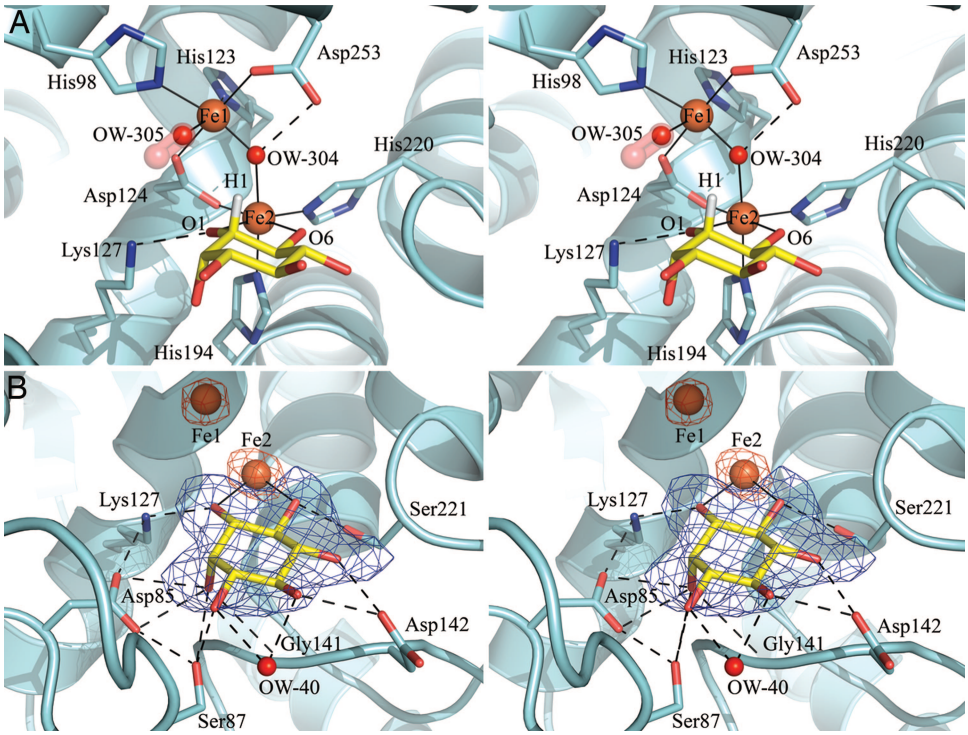

Fig. 3. Active site of MIOX. (*A*) Stereoview of the di-iron site. Fe atoms, orange spheres; MI, yellow; protein side chains in stick mode, colored by atom type; water/hydroxide ligands, red spheres. Bonds to Fe, solid lines; hydrogen bonds, broken lines. Note the change in helix geometry (α to 3_{10}) associated with His-123 and Asp-124. The C1 hydrogen of MI (gray) is adjacent to the modeled dioxygen (transparent orange spheres), in position for abstraction. (*B*) Stereoview of MI-binding mode. The Fe atoms, MI, side chains, water molecules, and hydrogen bonds are represented as in *A*. Electron density for MI is from a bias-removed omit map, contoured at 3σ, and the anomalous density for each Fe atom from the Fe-edge data is contoured at 7σ.

ate substrate specificity, are all invariant. To test the importance of these residues for function, we mutated each of Asp-85, Lys-127, Asp-142, and Ser-221 to Ala. The mutant proteins D85A, K127A, D142A, and S221A were all inactive, suggesting that the correct recognition and binding of MI is critical.

Sequence and Structure Comparisons. The current sequence database contains >40 putative MIOX sequences, from animals, plants, and microorganisms. Sequence comparisons (see Fig. 5, which is published as supporting information on the PNAS web site) show very high conservation. Mouse MIOX shares ≈90% identity with the human and rat enzymes and ≈45% identity with bacterial MIOXs, and even across 40 species, 43 residues are invariant. Most are involved in the di-iron site or the substrate-binding pocket, but some are remote from these sites (e.g., a cluster comprising Glu-104, Arg-107, Tyr-270, and Tyr-271) and may reflect other aspects of MIOX function. Between residues 38 and 281 there are only two positions where significant insertions or deletions occur in any MIOX sequence, implying high structural conservation.

Searches of the Protein Data Bank with SSM (28) show that the closest structural matches to MIOX are not any of the well known di-iron oxygenases, such as RNR (20) or MMO (21), but three uncharacterized proteins, from *Pyrococcus furiosus* (PDB code 1XX7), *Archaeoglubus fulvida* (PDB code 1YNB) and *E. coli* (PDB code 1WPH). Approximately 100 residues of MIOX can be superimposed onto each of these proteins (Fig. 2*B*) with root-mean-square differences in Cα positions of 2.8–3.2 Å. Correspondence is limited to helices α3, α4, α5, and parts of α6 and α8. Significantly, α4, α5, and α8 provide the ligands for FE(1) in MIOX (His-98, His-123, Asp-124, and Asp-253), and there are exact equivalents of each of these residues in the three microbial proteins, one of which (1XX7) binds a Ni^{2+} ion. A similar level of structural homology is found with the metal-binding catalytic domain of phosphodiesterases (29) and a domain from an exopolyphosphatase (30), and it is clear that all these proteins belong, with MIOX, to the HD-domain superfamily of metal-binding phosphohydrolases (22).

Despite the absence of significant sequence identity between MIOX and the HD-domain proteins (<5% overall), structural conservation suggests that they are related by divergence from a common ancestor. Key common elements are the antiparallel pair of helices α4/α5, which provide three metal ligands including the HD motif, plus α8, which provides a fourth ligand. These give rise to a metal-binding sequence His-$X_{\approx 30}$-His-Asp-$X_{>50}$-Asp, which coordinates FE(1) in MIOX and the Zn in phosphodiesterases. The HD motif is associated with a characteristic distortion of helix α5 that allows both residues to be presented together as metal ligands. At this position, the Asp residue has (φ, Ψ) angles (−100°, 20°), and helix α5 either terminates or changes to 3_{10}-type hydrogen bonding. Helices equivalent to α3, α6, and α7 in MIOX are present in the other HD-domain proteins but are more variable in their orientations compared with the core of α4, α5, and α8. Of the characterized HD-domain proteins, only in MIOX does the α6/α7 pair provide ligands for a second metal ion, FE(2); in phosphodiesterases the second metal has mostly water ligands and is displaced relative to FE(2). Other features unique to MIOX are the lid over the substrate provided by the α3–α4 loop and the complex loop region, which separates α4/α5 from α6/α7 and may play a role in protein–protein interactions by MIOX.

Discussion

Iron-dependent oxygenases are increasingly recognized for their key roles in a variety of essential biological processes (31, 32), reflecting the importance of iron for the binding and activation of molecular oxygen. Many contain a single iron center, Fe(II) in its resting state (32), but the di-iron oxygenases potentially display a richer chemistry, and participate in processes as diverse as *de novo* DNA synthesis (RNR) (20), hydrocarbon hydroxylation (methane and toluene monooxygenases) (21, 33), and fatty acid biosynthesis (Δ^9 stearoyl-acyl carrier protein desaturase) (34). MIOX, described here, has unique structural and functional features that expand the known repertoire of di-iron oxygenases.

Structural Relationships. MIOX shares key design features with di-iron oxygenases such as RNR and MMO. In these proteins, as for MIOX, the di-iron site is deeply buried between two antiparallel helix pairs, which provide most of the iron ligands (31). Burial in such a site may help protect the cell against the potentially damaging radical and oxidizing species that are formed as intermediates. The oxygen carrier hemerythrin also has its di-iron site within a similar four-helix cluster (35); the only known exception so far is purple acid phosphatase, an α/β protein which does not bind molecular oxygen (36). Despite its design similarities, MIOX does not appear to be evolutionarily related to RNR, MMO, and Δ^9 desaturase. The latter group is characterized by a common set of iron ligands, including a repeated HxxD motif, and substantial structural homology (31, 34). MIOX, in contrast, lacks this HxxD motif and belongs to a structurally distinct family, the HD-domain superfamily (22), with its HD sequence signature and strongly conserved metal-binding structure.

The functional properties of proteins with di-iron sites are tuned by the protein ligands that coordinate the iron atoms. Thus, hemerythrin, an oxygen carrier, has five His ligands and two carboxylates coordinating its two Fe(II) ions (35). In contrast, the oxygenases RNR, MMO, and Δ^9 desaturase each have two His ligands and four carboxylate ligands (21, 31), with the higher proportion of negatively charged carboxylate ligands likely to stabilize high-valent intermediates such as the diferryl Fe(IV)–Fe(IV) species proposed for RNR and MMO (26, 31). With four His ligands and two carboxylates, MIOX more closely resembles hemerythrin than the RNR-type oxygenases, suggesting that the proposed mechanism involving a (superoxo)di-iron(III)/(III) intermediate (18) is more likely than intermediates involving higher-valent species.

MIOX also differs from other oxygenases in having a valence-localized Fe(II)/Fe(III) pair as its catalytically competent state (16). Among structurally characterized di-iron enzymes, the only mixed-valence example is purple acid phosphatase (36), but its ligand complement is different, and it is not an oxygenase. The oxidized MIOX structure does not identify which of the iron atoms is more likely to be Fe(II) in the mixed-valent state, but structural and mechanistic considerations, discussed below, suggest FE(1) as the likely Fe(II) site. It is probable that the protein ligands present in the Fe(II)/Fe(III) state are the same as in the Fe(III)/Fe(III) crystal structure. Carboxylate shifts (37, 38), in which carboxylate ligands shift between monodentate and bridging as the redox state changes, have been documented for RNR and MMO (31, 38) and contribute to the altered metal coordination in a mixed-valent form of MMO (38). Such changes seem less likely for MIOX, however. The monodentate Asp ligand coordinated to FE(1) has insufficient flexibility to bridge to FE(2) without disruption of the whole di-iron site, and it is similarly unlikely that the bridging Asp-124 becomes monodentate. The use of Asp residues rather than the more flexible Glu to provide carboxylate ligands, and the presence of four His ligands, are key features that should ensure a relatively rigid di-iron site.

Mechanistic Implications. The catalytic cycle for MIOX is unprecedented among di-iron oxygenases in that it carries out a full four-electron oxidation of its substrate, returning to its Fe(II)/Fe(III) resting state without need for an external reductant (9, 18). Spectroscopic studies have identified a key intermediate **G**, which is reached reversibly after dioxygen binding, and is formally a (superoxo)Fe(III)/Fe(III) species (18). This abstracts the C1 hydrogen of MI, thereby cleaving the C1–H bond and resulting in the

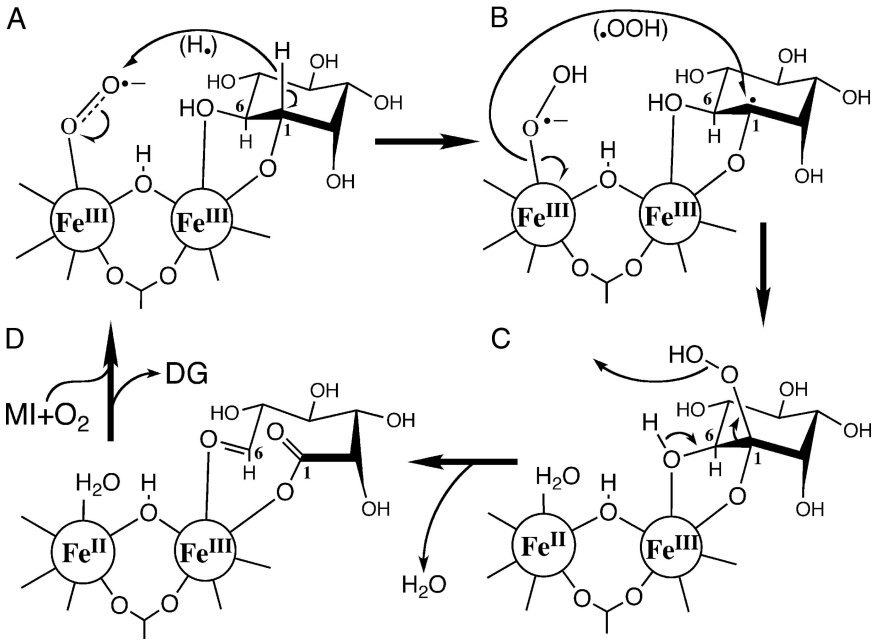

Fig. 4. Key steps in the MIOX reaction, following Xing *et al.* (18). (*A*) The putative (superoxo)Fe(III)/Fe(III) species, formed by displacement of the terminal water on FE(1) by dioxygen. Abstraction of the C1 H atom gives the radical species in *B*, followed by formation of a hydroperoxy derivative in *C*, breakage of the C1-C6 bond, and product release.

likely formation of a (hydroperoxo)Fe(III)/Fe(III) species, similar to the peroxodiiron(III) intermediate observed for toluene monooxygenase (39). Transfer of the intact hydroperoxide unit to the substrate C1 radical would then be followed by deprotonation of the C6 hydroxyl by a base to give an aldehyde at this position and breakdown of the hydroperoxy moiety with concomitant breakage of the C1–C6 bond (16, 18) (Fig. 4). The full sequence of steps is not clear, but the MIOX crystal structure illuminates several key points.

The structure confirms that the substrate binds directly to the di-iron moiety, as was deduced from substrate-induced spectroscopic changes (17), but the binding mode is fundamentally different from that suggested. Rather than bridging the irons via a μ-alkoxide bridge as proposed, MI binds in bidentate mode through its C1 and C6 hydroxyls, having major implications for the catalytic mechanism. The EPR spectra of the (superoxo)Fe(III)/Fe(III) intermediate **G** imply that oxygen binds to a single iron and not as a bridging species (18). Because no free coordination position exists on FE(2) for oxygen binding, we postulate that oxygen must bind to FE(1) by displacement of the terminal water ligand. Displacement of a protein ligand is unlikely, and oxygen is known to displace water ligands in other iron-dependent oxygenases. Each of the two iron atoms in MIOX thus has a different role, binding oxygen and substrate, respectively, and valence localization in the di-iron site thereby correlates with these distinct roles.

The substrate-binding mode strongly supports the proposed C–H cleavage mechanism (18). The C1 hydrogen is oriented toward the terminal water OW-305 on FE(1) (Fig. 3*A*) and is only 2.8 Å from it. Assuming that oxygen displaces OW-305, the resulting superoxo species would be ideally placed to abstract the C1 hydrogen as proposed. We modeled bound oxygen with end-on coordination (Fig. 3*A*) and find that it fits well in this orientation, adjacent to MI, although the general conclusions would not be altered by side-on binding. The observed MI-binding mode also clearly activates the substrate for attack. With four His ligands and two Asp, the Fe(II)/Fe(III) site has a formal net positive charge of 2+ or 3+, depending on whether the bridging aquo ligand is hydroxide or water. The coordination of the C1 hydroxyl to iron, and its strong hydrogen bond with the ε-amino group of Lys-127 (2.7 Å), will promote ionization of the C1 hydroxyl and help activate the C1–H bond for cleavage. Mutation of Lys-127 to Ala abolishes activity, consistent with this role. The C6 hydroxyl must also be deprotonated before formation of the C6 aldehyde (16). This process may also be assisted by coordination to iron, with the proton taken by the hydroxide liberated from the hydroperoxy unit or by the bridging hydroxide OW-304, 3.0 Å away from O6; this bridging species could act as a catalytic base, assisted by the noncoordinated carboxylate oxygen of Asp-253, to which it is hydrogen bonded.

Understanding all of the changes that occur at the di-iron center during the catalytic cycle will require multiple crystal structures for different states, as has been elegantly demonstrated for MMO (40). Those changes that do occur will likely involve the bridging species, especially the water/hydroxide. Binding of MI not only activates the substrate for attack, but also conditions the di-iron cluster for oxygen activation. The observed increase in Fe–Fe exchange coupling that accompanies MI binding (17) may result from conversion of bridging water to hydroxide. It is also possible that, in the absence of substrate, this aquo species does not bridge and that an additional consequence of MI binding is to bring the two iron atoms closer together.

Implications for Substrate Specificity and Inhibitor Design. The biochemistry of diabetic complications is complex, and many therapeutic strategies have been discussed (41). Although linkages between inositol metabolism and diabetic complications are mostly circumstantial, the demonstrated therapeutic potential of inositol administration (5–7) suggests that the regulation of inositol levels may represent a useful strategy. Inhibition of MIOX, as the first enzyme in the only known pathway for inositol catabolism, should raise inositol levels in diabetes and may thus help counter hyperglycemia.

The crystal structure of MIOX explains its substrate specificity and provides a template for inhibitor design. Iron chelation through O1 and O6 implies that the configuration at C1 and C6 is likely critical for the correct alignment of the substrate with the iron-bound oxygen. The close fit of MI against residues 140–142,

conserved as VGD in all MIOX sequences, also restricts the substrate configuration at C4, whereas the configurations at C2, C3, and C5 appear much less restricted. Modeling shows that DCI, which differs from MI only in its configuration at C3, should bind in the same way as MI, with its axial C3 hydroxyl then able to interact with the side chains of Asp-88 and Lys-257. The restrictions at C4 also suggest that L-*chiro* inositol, which differs in configuration at C3, C4, and C5, may not be a substrate. Finally, if the observed MI-binding mode is taken as a template for inhibitor design, the axial substituents on C3 and C5 should offer attractive sites for derivatization, because they are oriented toward a cavity containing several water molecules.

Materials and Methods

Cloning, Expression, and Purification. The ORF encoding mouse MIOX was amplified by PCR from genomic DNA and cloned into the expression vector pPro-EX Htb (Invitrogen, Carlsbad, CA). This construct was transformed into *E. coli* BL21 (DE3) pRP cells, and the protein was expressed at 28°C and purified as described (23). Ni^{2+}-affinity chromatography, using the N-terminal His_6 tag, was followed by cleavage of the tag with recombinant tobacco etch virus protease. After incubation with 1 mM Fe^{2+} and a final step of size-exclusion chromatography, homogeneous fractions identified by dynamic light scattering were pooled and concentrated to 20 $mg{\cdot}ml^{-1}$. Mutant proteins D85A, D124A, K127A, D142A, and S221A were generated by PCR mutagenesis of the wild-type *MIOX* gene and expressed and purified as for wild type. Enzyme activity was measured by the colorimetric orcinol assay for D-glucuronate formation (25). Before crystallization, the enzyme was incubated with 20 mM MI.

Crystallization and Data Collection. Crystallization conditions were identified as described (23). Crystals grew from a 1:1 mixture of protein solution [20 $mg{\cdot}ml^{-1}$ MIOX/20 mM MI/50 mM Mes, pH 6.0/50 mM NaCl/2 mM Tris(2-carboxyethyl)-phosphine hydrochloride] and precipitant (4.4 M sodium formate). These crystals were orthorhombic, space group $P2_12_12_1$, with unit cell dimensions $a = 44.60$, $b = 77.20$, $c = 85.40$ Å, with one MIOX molecule in the asymmetric unit ($V_M = 2.2$ $Å^3{\cdot}Da^{-1}$). A mercury derivative was prepared by soaking crystals in mother liquor containing 5 mM methylmercuric chloride and then back-washing in mother liquor before data collection.

X-ray diffraction data were collected from crystals flash-frozen in liquid nitrogen after soaking in cryoprotectant [4.4 M sodium formate and 5% (vol/vol) ethylene glycol] for 15 s. Data were collected at 100 K on beamline ID-29 at the European Synchrotron Radiation Facility (Grenoble, France). Native data were collected at the Fe–Kα absorption edge to maximize anomalous scattering from the intrinsic iron atoms and at a remote wavelength, and mercury derivative data were collected at the Hg absorption edge. A second, high-resolution, native data set was collected at 100 K on beamline 9-2 at the Stanford Synchrotron Radiation Laboratory (Stanford, CA) and used for structure refinement. Diffraction data were integrated and scaled with MOSFLM and SCALA from the CCP4 program suite (42); statistics are in Table 1.

Structure Determination and Refinement. Phases were determined by using single isomorphous replacement with anomalous scattering phases from the mercury derivative supplemented with single-wavelength anomalous diffraction phases from the two intrinsic iron atoms. Heavy atom positions were located and refined with AUTOSHARP (43). Initial phases to 2.6 Å were improved and extended to 2.0 Å when the higher-resolution native data became available. The resulting electron-density map showed clear secondary structure, allowing building of a polyAla model using COOT (44), and subsequent sequence assignment. The two intrinsic Fe atoms were found at peak heights of 15σ and 12σ in anomalous-difference maps using the Fe K-edge peak data. The protein model was refined with REFMAC5 (45) and validated with PROCHECK (24). Restraints for MI were generated by using the Dundee PRODRG server (46). The bound MI molecule was clearly visible at a height of 5σ in the first experimentally phased maps. The final model contains residues 29–285, two iron atoms, one MI molecule, a hydroxide ion, 155 water molecules, and a formate ion. Figures were prepared with PyMOL (47).

We thank Fasseli Coulibaly, Richard Bunker, and Clyde Smith for help with data collection and Geoff Jameson and Anthony Phillips for useful discussions. This work was supported by the Maurice Wilkins Centre for Molecular Biodiscovery, the Health Research Council of New Zealand, Protemix Inc. (Auckland), and the Foundation for Research, Science and Technology through an Enterprise Scholarship (to P.M.B.).

1. Ostlund RE, Jr, McGill JB, Herskowitz I, Kipnis DM, Santiago JV, Sherman WR (1993) *Proc Natl Acad Sci USA* 90:9988–9992.
2. Asplin I, Galasko G, Larner J (1993) *Proc Natl Acad Sci USA* 90:5924–5928.
3. Kawa JM, Przybylski R, Taylor CG (2003) *Exp Biol Med* 228:907–914.
4. Frick W, Bauer A, Bauer J, Wied S, Muller G (1998) *Biochem J* 336:163–181.
5. Nascimento NR, Lessa LM, Kerntopf MR, Sousa CM, Alves RS, Queiroz MG, Price J, Heimark DB, Larner J, Du X, *et al.* (2006) *Proc Natl Acad Sci USA* 103:218–223.
6. Ortmeyer HK, Bodkin NL, Lilley K, Larner J, Hansen BC (1993) *Endocrinology* 132:640–645.
7. Brautigan DL, Brown M, Grindrod S, Chinigo G, Kruszewski A, Lukasik SM, Bushweller JH, Horal M, Keller S, Tamura S, *et al.* (2005) *Biochemistry* 44:11067–11073.
8. Charalampous FC (1959) *J Biol Chem* 234:220–227.
9. Moskala R, Reddy CC, Minard RD, Hamilton GA (1981) *Biochem Biophys Res Commun* 99:107–113.
10. Hankes LV, Politzer WM, Touster O, Anderson L (1969) *Ann NY Acad Sci* 165:564–576.
11. Arner RJ, Prabhu KS, Krishnan V, Johnson MC, Reddy CC (2006) *Biochem Biophys Res Commun* 339:816–820.
12. Arner RJ, Prabhu KS, Thompson JT, Hildenbrandt GR, Liken AD, Reddy CC (2001) *Biochem J* 360:313–320.
13. Nayak B, Xie P, Akagi S, Yang Q, Sun L, Wada J, Thakur A, Danesh FR, Chugh SS, Kanwar YS (2005) *Proc Natl Acad Sci USA* 102:17952–17957.
14. Prabhu KS, Arner RJ, Vunta H, Reddy CC (2005) *J Biol Chem* 280:19895–19901.
15. Arner RJ, Prabhu KS, Reddy CC (2004) *Biochem Biophys Res Commun* 324:1386–1392.
16. Xing G, Barr EW, Diao Y, Hoffart LM, Prabhu KS, Arner RJ, Reddy CC, Krebs C, Bollinger JMJ (2006) *Biochemistry* 45:5402–5412.
17. Xing G, Hoffart LM, Diao Y, Prabhu KS, Arner RJ, Reddy CC, Krebs C, Bollinger JMJ (2006) *Biochemistry* 45:5393–5401.
18. Xing G, Diao Y, Hoffart LM, Barr EW, Prabhu KS, Arner RJ, Reddy CC, Krebs C, Bollinger JMJ (2006) *Proc Natl Acad Sci USA* 103:6130–6135.
19. Yang Q, Dixit B, Wada J, Tian Y, Wallner EI, Srivastva SK, Kanwar YS (2000) *Proc Natl Acad Sci USA* 97:9896–9901.
20. Nordlund P, Sjoberg B-M, Eklund H (1990) *Nature* 345:593–598.
21. Rosenzweig AC, Frederick CA, Lippard SJ, Nordlund P (1993) *Nature* 366:537–543.
22. Aravind L, Koonin EV (1998) *Trends Biochem Sci* 23:469–472.
23. Brown PM, Caradoc-Davies TT, Dickson JM, Loomes KM, Baker EN (2006) *Acta Crystallogr F* 62:811–813.
24. Laskowski RA, MacArthur MW, Moss DS, Thornton JM (1993) *J Appl Crystallogr* 26:283–291.
25. Reddy CC, Swan JS, Hamilton GA (1981) *J Biol Chem* 256:8510–8518.
26. Solomon EI, Brunold TC, Davis MI, Kemsley JN, Lee S-K, Lehnert N, Neese F, Skulan AJ, Yang Y-S, Zhou J (2000) *Chem Rev* 100:235–349.
27. Kurtz DM, Jr (1990) *Chem Rev* 90:585–606.
28. Krissinel E, Henrick K (2004) *Acta Crystallogr D* 60:2256–2268.
29. Xu RX, Hassell AM, Vanderwall D, Lambert MH, Holmes WD, Luther MA, Rocque WJ, Milburn MV, Zhao Y, Ke H, Nolte RT (2000) *Science* 288:1822–1825.
30. Alvarado J, Ghosh A, Janovitz T, Jauregui A, Hasson MS, Sanders DA (2006) *Structure (London)* 14:1263–1272.
31. Nordlund P, Eklund H (1995) *Curr Opin Struct Biol* 5:758–766.
32. Ryle MJ, Hausinger RP (2002) *Curr Opin Chem Biol* 6:193–201.
33. Sazinsky MH, Bard J, Di Donato A, Lippard SJ (2004) *J Biol Chem* 279:30600–30610.
34. Lindqvist Y, Huang W, Schneider G, Shanklin J (1996) *EMBO J* 15:4081–4092.
35. Holmes MA, Stenkamp RE (1991) *J Mol Biol* 220:723–737.
36. Guddat LW, McAlpine AS, Hume D, Hamilton S, De Jersey J, Martin JL (1999) *Structure (London)* 7:757–767.
37. Rardin RL, Tolman WB, Lippard SJ (1991) *New J Chem* 15:417–430.
38. Whittington DA, Lippard SJ (2001) *J Am Chem Soc* 123:827–838.
39. Merkx M, Kopp DA, Sazinsky MH, Blazyk JL, Muller J, Lippard SJ (2001) *Angew Chem Int Ed* 40:2782–2807.
40. Murray LJ, Garcia-Serres R, Naik S, Huynh BH, Lippard SJ (2006) *J Am Chem Soc* 128:7458–7459.
41. Brownlee M (2001) *Nature* 414:813–820.
42. Collaborative Computational Project Number 4 (1994) *Acta Crystallogr D* 50:760–763.
43. de La Fortelleqq E, Bricogne G (1997) *Methods Enzymol* 276:472–494.
44. Emsley P, Cowtan K (2004) *Acta Crystallogr D* 60:2126–2132.
45. Murshudov GN, Vagin AA, Dodson EJ (1997) *Acta Crystallogr D* 53:240–255.
46. Schuettelkopf AW, van Aalten DMF (2004) *Acta Crystallogr D* 60:1355–1363.
47. DeLano WL (2002) PyMOL (DeLano Scientific, San Carlos, CA).